Delft University of Technology

Online Inertial Measurement Unit Fault Identification and Active Fault-Tolerant Flight Control

Authors
Atmaca, Direnc; Visser, Coen de; Kampen, Erik-Jan van

DOI
10.2514/1.G009147

Publication date
2025

Document Version
Final published version

Published in
Journal of Guidance, Control, and Dynamics

Citation (APA)
Atmaca, D., Visser, C. D., & Kampen, E.-J. V. (2025). Online Inertial Measurement Unit Fault Identification and Active Fault-Tolerant Flight Control. *Journal of Guidance, Control, and Dynamics*, *48*(10), 2389-2398. https://doi.org/10.2514/1.G009147

JOURNAL OF GUIDANCE, CONTROL, AND DYNAMICS

Technical Notes

Online Inertial Measurement Unit Fault Identification and Active Fault-Tolerant Flight Control

Direnc Atmaca,[*] Coen de Visser,[†] and
Erik-Jan van Kampen[‡]
Delft University of Technology, 2629 HS Delft,
The Netherlands

https://doi.org/10.2514/1.G009147

I. Introduction

MODERN aircraft rely heavily on a wide array of sensors for navigation and flight control, including air-data, Global Positioning System (GPS), and inertial sensors. Proper functioning of such sensors is crucial for maintaining flight safety. Hence, in-flight identification and correction of potential sensor faults constitutes an important topic in aerospace. The typical industry approach to sensor fault identification (FI) is through hardware redundancy [1]. A monitoring algorithm compares redundant sensors to detect and isolate the source of the fault and prevents the use of faulty data in flight control computers. However, ensuring safety with hardware redundancy increases the overall cost and weight of an aircraft, which are typically under strict constraints [2]. In addition, some recent flight accidents show that hardware redundancy has limitations [3–5]. In 2023, a military jet crashed on the western coast of South Korea due to GPS and inertial measurement unit (IMU) failure [3]. In another incident [4,5], the failure of the air-data inertial reference unit caused a flight upset that injured 11 passengers. Consequently, these incidents emphasize the need to explore alternative methods for IMU sensor FI.

The search for alternative approaches led to the development of analytical redundancy methods, which are subcategorized as model-based and data-driven [2]. Some recent studies focus on aircraft IMU FI using model-based techniques, employing deterministic and stochastic methods [6–10]. Most of these papers utilize a nonlinear kinematic process model to eliminate the impact of aerodynamic model uncertainties on state and fault estimation. The state and details of various fault identification techniques developed in the last two decades are available in [1,2,11,12].

This Note provides three primary contributions. First, it introduces a novel fault identification and state estimation strategy for step, incipient, and oscillatory IMU faults by combining an optimal two-stage extended Kalman filter (OTSEKF) [13] and a higher-order sliding mode (HOSM) differentiator [14–16]. This combination tackles two important problems in the IMU FI framework, which are noise amplification and sensitivity to initial conditions. As Sec. III.B explains, the flatness property of systems allows demonstrating that IMU faults are related to the drift in state variables through first-order differentiation and algebraic relations. As a result, this enables the identification of IMU faults by differentiating the drift in state variables. However, since differentiation amplifies noise, the use of the HOSM differentiator facilitates noise rejection and provides accurate IMU fault estimates. Furthermore, incorporating sliding mode reduces the sensitivity of OTSEKF to initial conditions [17]. In previous research [18], OTSEKF has been shown to be highly sensitive to initial conditions due to the linearization of the filter, leading to large deviations in fault estimates. The existing solution to this problem is to use an "iterated" linearization step. However, although this improves the performance, it does not solve the issue completely and adds computational load. Conversely, using a nonrecursive and algebraic HOSM structure solves this problem with minimal computational burden. This makes OTSEKF-HOSM a powerful combination for online state estimation and fault identification.

Secondly, it proposes an active sensor fault-tolerant control system for a flying-wing aircraft by combining the introduced IMU FI strategy with incremental nonlinear dynamic inversion (INDI). Since INDI controllers require accurate rate gyro measurements, uncorrected IMU faults can cause performance degradation. In this approach, IMU faults identified through the OTSEKF-HOSM are used to correct IMU measurements and to maintain the performance of the INDI controller. The INDI and the aircraft outer loop controllers both use the states estimated with the OTSEKF under IMU faults.

Lastly, this study considers turbulence as a perturbing effect. To this end, it utilizes a kinematic model based on ground speed that accounts for changing wind for state and fault estimation. This improves the suitability of the method for real-life implementation. In earlier research, a similar kinematic model was used to account for wind in offline simulations [8]. However, this Note proposes a modified approximate kinematic model that uses fault estimates and incorporates wind in-flight.

The rest of the Note is structured as follows: Section II outlines the approximate kinematic model with IMU faults. Section III introduces the IMU FI structure that includes the optimal two-stage extended Kalman filter and the higher-order sliding mode differentiator. Section IV presents the IMU FI results under turbulent flight conditions. Section V discusses the active sensor fault-tolerant control structure and presents a performance comparison. Lastly, Sec. VI provides the conclusions and reiterates key findings.

II. Approximate Aircraft Kinematic Model with IMU Faults

The kinematic model used for state and fault estimation is based on ground speed to account for turbulence. In the past, a similar kinematic model with exact process equations has been proposed for the same purpose [8]. However, this section offers a modified kinematic model with nonexact process equations that accounts for the wind, performs fault observation, and minimizes couplings between IMU faults.

A general nonlinear aircraft kinematic model can be written as the following:

$$\dot{\boldsymbol{x}} \approx \boldsymbol{f}(\boldsymbol{x}(t), \boldsymbol{u}_m(t), \hat{\boldsymbol{f}}^i(t)) + \mathbf{G}(\boldsymbol{x}(t))\boldsymbol{\omega}(t) \tag{1}$$

$$\boldsymbol{y}_m(t) = \boldsymbol{h}(\boldsymbol{x}(t), \boldsymbol{u}_m(t), t) + \boldsymbol{\nu}(t) \tag{2}$$

where $\boldsymbol{x}$ denotes the state vector, $\boldsymbol{u}_m$ represents the measured input to the system, $\hat{\boldsymbol{f}}^i$ indicates the estimated input faults, $\boldsymbol{y}_m$ signifies the

---

Received 26 February 2025; accepted for publication 24 June 2025; published online 17 July 2025. Copyright © 2025 by Delft University of Technology. Published by the American Institute of Aeronautics and Astronautics, Inc., with permission. All requests for copying and permission to reprint should be submitted to CCC at www.copyright.com; employ the eISSN 1533-3884 to initiate your request. See also AIAA Rights and Permissions https://aiaa.org/publications/publish-with-aiaa/rights-and-permissions/.

[*] Ph.D. Candidate, Control and Simulation, Faculty of Aerospace Engineering, Kluyverweg 1; d.atmaca@tudelft.nl (Corresponding Author).

[†] Associate Professor, Control and Simulation, Faculty of Aerospace Engineering, Kluyverweg 1; c.c.devisser@tudelft.nl.

[‡] Associate Professor, Control and Simulation, Faculty of Aerospace Engineering, Kluyverweg 1; e.vankampen@tudelft.nl.

measured output, $\mathbf{G}$ is the noise distribution matrix, $\boldsymbol{h}$ is the measurement model, and $\boldsymbol{\omega}$ and $\boldsymbol{\nu}$ are zero-mean Gaussian input and measurement noise vectors, respectively. All variables are contained in $\mathbb{R}$. For this modified kinematic model based on ground speed with IMU faults, these variables are expressed as follows [8]:

$$\boldsymbol{x} = \begin{bmatrix} u^b_{GS} & v^b_{GS} & w^b_{GS} & \phi & \theta & \psi \end{bmatrix}^T \tag{3}$$

$$\begin{aligned} \boldsymbol{u}_m &= \begin{bmatrix} A_{xm} & A_{ym} & A_{zm} & p_m & q_m & r_m \end{bmatrix}^T \\ &= \begin{bmatrix} A_x & A_y & A_z & p & q & r \end{bmatrix}^T + \boldsymbol{\omega} + \boldsymbol{f}^i \end{aligned} \tag{4}$$

$$\begin{aligned} \boldsymbol{y}_m &= \begin{bmatrix} u_{GS_m} & v_{GS_m} & w_{GS_m} & \phi_m & \theta_m & \psi_m \end{bmatrix}^T \\ &= \begin{bmatrix} u_{GS} & v_{GS} & w_{GS} & \phi & \theta & \psi \end{bmatrix}^T + \boldsymbol{\nu} \end{aligned} \tag{5}$$

$$\boldsymbol{f}^i = \begin{bmatrix} f_{Ax} & f_{Ay} & f_{Az} & f_p & f_q & f_r \end{bmatrix}^T \tag{6}$$

$$\boldsymbol{\omega} = \begin{bmatrix} \omega_{A_x} & \omega_{A_y} & \omega_{A_z} & \omega_p & \omega_q & \omega_r \end{bmatrix}^T \tag{7}$$

$$\boldsymbol{\nu} = \begin{bmatrix} \nu_{u_{GS}} & \nu_{v_{GS}} & \nu_{w_{GS}} & \nu_\phi & \nu_\theta & \nu_\psi \end{bmatrix}^T \tag{8}$$

where u^b_{GS}, v^b_{GS}, and w^b_{GS} are the components of the ground speed expressed in the body frame; ϕ, θ, and ψ are the attitude angles; A_x, A_y, and A_z are the true linear accelerations; p, q, and r are the true rotational rates; and u_{GS_m}, v_{GS_m}, and w_{GS_m} are the GPS ground speed measurements. Based on this set of definitions, the measured input is expressed as a linear combination of true values, IMU sensor noise, and true IMU faults. The input faults for the IMU sensors are contained in $\boldsymbol{f}^i$.

Now that the system is fully defined, the next step is developing the process model. In previous studies focusing on state and fault identification problems [8–10,19], the process models have been defined as exact. However, defining the exact equations requires complete knowledge of IMU faults, which is unrealistic because if real fault information is readily available, the fault identification process becomes unnecessary. Instead, this section proposes a modified kinematic model with nonexact process equations that utilizes fault estimates, which is given as follows:

$$\dot{u}^b_{GS} \approx v^b_{GS}(r_m - \hat{f}_r) - w^b_{GS}(q_m - \hat{f}_q) + A_{xm} - g\sin\theta \tag{9}$$

$$\dot{v}^b_{GS} \approx -u^b_{GS}(r_m - \hat{f}_r) + w^b_{GS}(p_m - \hat{f}_p) + A_{ym} + g\cos\theta\sin\phi \tag{10}$$

$$\dot{w}^b_{GS} \approx u^b_{GS}(q_m - \hat{f}_q) - v^b_{GS}(p_m - \hat{f}_p) + A_{zm} + g\cos\theta\cos\phi \tag{11}$$

$$\dot{\phi}_p \approx p_m + (q_m - \hat{f}_q)\sin\phi\tan\theta + (r_m - \hat{f}_r)\cos\phi\tan\theta \tag{12}$$

$$\dot{\theta}_p \approx q_m\cos\phi - (r_m - \hat{f}_r)\sin\phi \tag{13}$$

$$\dot{\psi}_p \approx (q_m - \hat{f}_q)\frac{\sin\phi}{\cos\theta} + r_m\frac{\cos\phi}{\cos\theta} \tag{14}$$

One reason for constructing the model this way is for separating the fault contribution of each IMU sensor to each state variable. For example, looking at Eq. (9), it is possible to notice that estimate fault contributions $\hat{f}_r$ and $\hat{f}_q$ are subtracted from their corresponding IMU sensor measurements, whereas $\hat{f}_{Ax}$ is not subtracted and is contained in A_{xm}. This ensures that the drift in the state variable $\dot{u}^b_{GS}$ is predominantly caused by $\hat{f}_{Ax}$ and not by the faults in other sensors, which minimizes the coupling between IMU faults and holds as long as the estimated faults closely match the true faults, $\hat{f} \approx f$. All process equations follow the same structure. The IMU fault driving the drift in the ground speed components is preserved in the accelerometer measurements A_{xm}, A_{ym}, and A_{zm}, while it is retained in the rate gyro measurements p_m, q_m, and r_m, for the attitude angles.

Fundamentally, by structuring the model this way, the predicted states are allowed to drift in a restricted way compared to the true or measured states. This may seem counterintuitive at first, but as explained in the next section, the drift in predicted states plays an important role within the optimal two-stage extended Kalman filter framework. This is because the fault information enters into the system as a drift in state variables, which follows from Eq. (20) as $\bar{\boldsymbol{x}}_{k|k-1}$ is allowed to drift before being corrected in the subsequent stages of the filter. To complete the system definition, the noise distribution matrix and the measurement model are defined as follows [8]:

$$\mathbf{G}(\boldsymbol{x}(t)) = \begin{bmatrix} -1 & 0 & 0 & 0 & w^b_{GS} & -v^b_{GS} \\ 0 & -1 & 0 & -w^b_{GS} & 0 & u^b_{GS} \\ 0 & 0 & -1 & v^b_{GS} & -u^b_{GS} & 0 \\ 0 & 0 & 0 & -1 & -\sin\phi\tan\theta & -\cos\phi\tan\theta \\ 0 & 0 & 0 & 0 & -\cos\phi & \sin\phi \\ 0 & 0 & 0 & 0 & -\sin\phi/\cos\theta & -\cos\phi/\cos\theta \end{bmatrix} \tag{15}$$

$$\begin{aligned} \begin{bmatrix} u_{GS_m} & v_{GS_m} & w_{GS_m} \end{bmatrix}^T &= T_{EB}\begin{bmatrix} u^b_{GS} & v^b_{GS} & w^b_{GS} \end{bmatrix}^T \\ &\quad + \begin{bmatrix} \nu_{u_{GS}} & \nu_{v_{GS}} & \nu_{w_{GS}} \end{bmatrix}^T \end{aligned} \tag{16}$$

$$\phi_m = \phi + \nu_\phi \tag{17}$$

$$\theta_m = \theta + \nu_\theta \tag{18}$$

$$\psi_m = \psi + \nu_\psi \tag{19}$$

where T_{EB} is a transformation matrix that converts the body frame into the Earth-centered, Earth-fixed (ECEF) frame under the assumption that Earth is flat and nonrotating.

III. IMU FI Framework

This section introduces the complete IMU fault identification strategy that utilizes the nonlinear aircraft kinematic model. The strategy simultaneously addresses the state estimation problem under time-varying IMU faults and reconstructs them. State estimation is performed through an optimal two-stage extended Kalman filter (OTSEKF), whereas a higher-order sliding mode (HOSM) differentiator complements the OTSEKF and reconstructs the IMU faults. Figure 1 gives the schematic of this framework. In this figure, $\boldsymbol{f}^i$ indicates the true IMU faults; $\bar{\boldsymbol{x}}_{k|k-1}$ and $\bar{\boldsymbol{x}}_{k|k}$, respectively, represent the predicted and corrected states under IMU faults without treating the faults, which means that the states are allowed to drift at this step; $\hat{\boldsymbol{\mu}}^i$ denotes the estimated drift in state variables; $\hat{\boldsymbol{x}}_{k|k}$ signifies the final

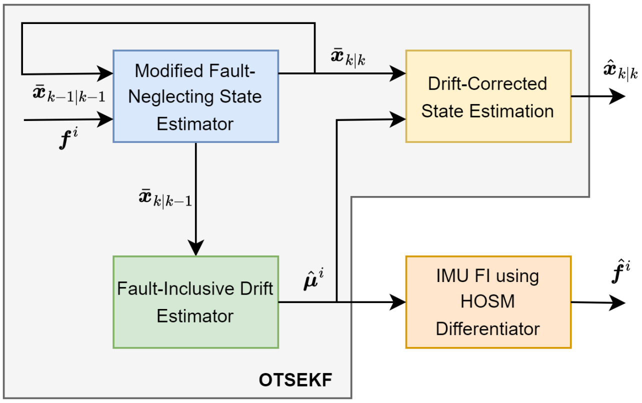

Fig. 1 Schematic of the fault identification framework.

drift-corrected state estimate; and $\hat{\boldsymbol{f}}^i$ symbolizes the estimated IMU faults. Note that in reality, the modified fault-neglecting state estimator and fault-inclusive drift estimator run in parallel; they only appear here sequentially for the sake of demonstration.

A. Optimal Two-Stage Extended Kalman Filter

This Note essentially addresses an input fault identification problem since the IMU measurements act as inputs to the nonlinear kinematic model. In the Kalman filter framework, the typical way to deal with this is to consider faults or biases as part of the system state and to perform the state and parameter estimation simultaneously in a single stage, leading to the augmented state Kalman filter (ASKF). However, this causes a large state vector and, consequently, high computational complexity, i.e., $\mathcal{O}((n+b)^3)$, where n is the dimension of the states and b of the faults [8]. Friedland [20] proposes decomposing the single-stage filter into two parallel filters as a separate fault-free state estimator and a state drift estimator. Although this reduces the computational complexity to $\mathcal{O}(n^3+b^3)$, the decomposition of the filter is only optimal for constant faults. In case of random or time-varying faults, the decomposition is only optimal if the correlation between the state and fault noises satisfies an algebraic constraint [21]. Keller and Darouach [22] provide a formulation that is able to optimally decouple the filter under time-varying faults by using a modified fault-free state estimator. Under constant faults, this structure is equivalent to that of Friedland's. Following this, Hsieh and Chen [13] derive an optimal two-stage Kalman filter (OTSKF) in the minimum mean square error sense that eliminates the necessity of satisfying the algebraic constraint and is stable as long as the modified fault-free state covariance matrix $\overline{\mathbf{Q}}_{k-1}$ is positive semidefinite. Many other researchers contributed to the extension of Friedland's two-stage formulation to nonlinear systems [23–26]. Some of them even showed earlier applications to fault-tolerant navigation [27,28] and target tracking problems [29].

This Note adopts the structure proposed by [13] for the OTSEKF part of the IMU FI framework, which is also used in [8]. This later is combined with a HOSM differentiator to minimize sensitivity to initial conditions and to obtain accurate fault estimates through differentiation. The equations used in this section are mainly based on [8] and are modified where necessary for the purposes of this work.

1. *Modified Fault-Neglecting State Estimator*

This first part of the OTSEKF performs state prediction while neglecting the input faults that exist in the IMU measurements. It is given by the following set of equations, based on [8]:

$$\bar{\boldsymbol{x}}_{k|k-1} = \bar{\boldsymbol{x}}_{k-1|k-1} + \int_{t_{k-1}}^{t_k} \boldsymbol{f}(\bar{\boldsymbol{x}}(t), \boldsymbol{u}_m(t), \mathbf{0}, t)\,\mathrm{d}t + \bar{\boldsymbol{u}}_{k-1} \tag{20}$$

$$\bar{\boldsymbol{x}}_{k|k} = \bar{\boldsymbol{x}}_{k|k-1} + \boldsymbol{K}_k^{\bar{x}}(\boldsymbol{y}_{m,k} - \mathbf{H}_k\bar{\boldsymbol{x}}_{k|k-1}) \tag{21}$$

$$\mathbf{P}_{k|k-1}^{\bar{x}} = \boldsymbol{\Phi}_{k-1}\mathbf{P}_{k-1|k-1}^{\bar{x}}\boldsymbol{\Phi}_{k-1}^T + \bar{\mathbf{Q}}_{k-1} \tag{22}$$

$$\boldsymbol{K}_k^{\bar{x}} = \mathbf{P}_{k|k-1}^{\bar{x}}\mathbf{H}_k^T(\mathbf{H}_k\mathbf{P}_{k|k-1}^{\bar{x}}\mathbf{H}_k^T + \mathbf{R}_k)^{-1} \tag{23}$$

$$\mathbf{P}_{k|k}^{\bar{x}} = (\mathbf{I} - \boldsymbol{K}_k^{\bar{x}}\mathbf{H}_k)\mathbf{P}_{k|k-1}^{\bar{x}} \tag{24}$$

where $\bar{\boldsymbol{x}}_{k|k-1}$ is the predicted state vector, $\boldsymbol{K}_k^{\bar{x}}$ is the state Kalman gain, and $\mathbf{P}_{k|k-1}^{\bar{x}}$ is the predicted state covariance matrix. Furthermore, the discrete system transition matrix $\boldsymbol{\Phi}_{k-1}$, the discrete noise distribution matrix $\boldsymbol{\Gamma}_{k-1}$, and the observation matrix $\mathbf{H}_k$ are defined as follows:

$$\boldsymbol{\Phi}_{k-1} = e^{\mathbf{F}_{k-1}\Delta t} = \sum_{n}^{\infty}\frac{\mathbf{F}_{k-1}^n(\Delta t)^n}{n!}, \ \Delta t = t_k - t_{k-1} \tag{25}$$

$$\mathbf{F}_{k-1} = \left.\frac{\partial \boldsymbol{f}(\boldsymbol{x}(t), \boldsymbol{u}_m(t), \mathbf{0})}{\partial \boldsymbol{x}}\right|_{\boldsymbol{x}=\hat{\boldsymbol{x}}_{k-1|k-1}}, \quad \mathbf{H}_k = \left.\frac{\partial \boldsymbol{h}(\boldsymbol{x}(t), \boldsymbol{u}_m(t))}{\partial \boldsymbol{x}}\right|_{\boldsymbol{x}=\hat{\boldsymbol{x}}_{k-1|k-1}} \tag{26}$$

$$\boldsymbol{\Gamma}_{k-1} = \int_{t_{k-1}}^{t_k} \boldsymbol{\Phi}_{k-1}\mathbf{G}(\bar{\boldsymbol{x}}_{k-1|k-1})\,\mathrm{d}t \tag{27}$$

$$\mathbf{Q}_k = E\{\boldsymbol{\omega}(t)^T\boldsymbol{\omega}(t)\}, \qquad \mathbf{R}_k = E\{\boldsymbol{\nu}(t)^T\boldsymbol{\nu}(t)\} \tag{28}$$

From these sets of equations, one may realize that the modified fault-neglecting state estimator is similar to the discrete formulation of the conventional extended Kalman filter. The difference comes from $\overline{\mathbf{Q}}_{k-1}$ and $\bar{\boldsymbol{u}}_{k-1}$, which are coupling terms that are outlined in the following subsections.

2. *Fault-Inclusive Drift Estimator*

The purpose of this part of the OTSEKF is to estimate the drift in the predicted states caused by IMU faults. For the ground speed-based kinematic model, the estimated drift is defined as the following:

$$\hat{\boldsymbol{\mu}}^i = \begin{bmatrix} \hat{\tilde{u}}_{GS}^b & \hat{\tilde{v}}_{GS}^b & \hat{\tilde{w}}_{GS}^b & \hat{\tilde{\phi}} & \hat{\tilde{\theta}} & \hat{\tilde{\psi}} \end{bmatrix}^T \tag{29}$$

The estimation of drift serves two purposes: firstly, to correct the predicted states that are allowed to drift during the first stage of the filter, thereby yielding final state estimates that are corrected for drift; secondly, for the reconstruction of IMU faults using a HOSM differentiator. The main equations of this section are modified from [8] and written as follows:

$$\hat{\boldsymbol{\mu}}_{k|k-1}^i = \hat{\boldsymbol{\mu}}_{k-1|k-1}^i \tag{30}$$

$$\mathbf{P}_{k|k-1}^{\boldsymbol{\mu}^i} = \mathbf{P}_{k-1|k-1}^{\boldsymbol{\mu}^i} + \mathbf{Q}_{k-1}^{\boldsymbol{\mu}^i} \tag{31}$$

$$\boldsymbol{K}_k^{\boldsymbol{\mu}^i} = \mathbf{P}_{k|k-1}^{\boldsymbol{\mu}^i}\mathbf{S}_k^T(\mathbf{H}_k\mathbf{P}_{k|k-1}^{\bar{x}}\mathbf{H}_k^T + \mathbf{R}_k + \mathbf{S}_k\mathbf{P}_{k|k-1}^{\boldsymbol{\mu}^i}\mathbf{S}_k^T)^{-1} \tag{32}$$

$$\hat{\boldsymbol{\mu}}_{k|k}^i = \hat{\boldsymbol{\mu}}_{k|k-1}^i + \boldsymbol{K}_k^{\boldsymbol{\mu}^i}(\boldsymbol{y}_{m,k} - \mathbf{H}_k\bar{\boldsymbol{x}}_{k|k-1} - \mathbf{S}_k\hat{\boldsymbol{\mu}}_{k|k-1}^i) \tag{33}$$

$$\mathbf{P}_{k|k}^{\boldsymbol{\mu}^i} = (\mathbf{I} - \boldsymbol{K}_k^{\boldsymbol{\mu}^i}\mathbf{S}_k)\mathbf{P}_{k|k-1}^{\boldsymbol{\mu}^i} \tag{34}$$

where $\mathbf{P}_{k|k-1}^{\boldsymbol{\mu}^i}$ is the fault covariance matrix, $\mathbf{K}_k^{\boldsymbol{\mu}^i}$ is the Kalman gain of the faults, and $\mathbf{Q}_{k-1}^{\boldsymbol{\mu}^i}$ is the fault noise covariance matrix. In addition, some auxiliary definitions are written as

$$\bar{\boldsymbol{u}}_k = (\bar{\mathbf{U}}_{k+1} - \mathbf{U}_{k+1})\hat{\boldsymbol{\mu}}_{k|k}^i \tag{35}$$

$$\bar{\mathbf{Q}}_k = \boldsymbol{\Gamma}_k\mathbf{Q}_k\boldsymbol{\Gamma}_k^T - \mathbf{Q}_k^{x\boldsymbol{\mu}^i}\bar{\mathbf{U}}_{k+1}^T - \mathbf{U}_{k+1}(\mathbf{Q}_k^{x\boldsymbol{\mu}^i} - \bar{\mathbf{U}}_{k+1}\mathbf{Q}_k^{\boldsymbol{\mu}^i})^T \tag{36}$$

$$\bar{\mathbf{U}}_k = \boldsymbol{\Phi}_{k-1}\mathbf{V}_{k-1} + \boldsymbol{\Gamma}_{k-1} \tag{37}$$

$$\mathbf{S}_k = \mathbf{H}_k\mathbf{U}_k \tag{38}$$

$$\mathbf{U}_k = \bar{\mathbf{U}}_k + (\mathbf{Q}_{k+1}^{x\boldsymbol{\mu}^i} - \bar{\mathbf{U}}_k\mathbf{Q}_{k-1}^{\boldsymbol{\mu}^i})(\mathbf{P}_{k|k-1}^{\boldsymbol{\mu}^i})^{-1} \tag{39}$$

$$\mathbf{V}_k = \mathbf{U}_k - \boldsymbol{K}_k^{\bar{x}}\mathbf{S}_k \tag{40}$$

where $\mathbf{U}_k$ and $\mathbf{V}_k$ are called blending matrices, while $\mathbf{Q}_k^{x\boldsymbol{\mu}^i}$ is the covariance matrix that describes the correlation between process and fault noise and is equal to zero in the case of constant faults. This completes the drift estimator. The following section combines the outputs of the modified fault-neglecting state estimator and the fault-inclusive drift estimator to obtain the final state estimate and its covariance.

3. *Drift-Corrected State Estimation*

This final stage combines the output of the first two stages and provides the corrected state estimates and its covariance, as written below [8]:

$$\hat{\boldsymbol{x}}_{k|k} = \bar{\boldsymbol{x}}_{k|k} + \mathbf{V}_k \hat{\boldsymbol{\mu}}^i_{k|k} \tag{41}$$

$$\mathbf{P}^{\boldsymbol{x}}_{k|k} = \mathbf{P}^{\bar{\boldsymbol{x}}}_{k|k} + \mathbf{V}_k \mathbf{P}^{\boldsymbol{\mu}^i}_{k|k} \mathbf{V}^T_k \tag{42}$$

From Eq. (41), it is possible to observe that the final corrected estimate is a linear combination of the modified fault-neglecting state estimator output, $\bar{\boldsymbol{x}}_{k|k}$, and the fault-inclusive drift estimator output, $\hat{\boldsymbol{\mu}}^i_{k|k}$. Hence, through the OTSEKF, the estimates are corrected for IMU faults without explicitly identifying them. The next section addresses the IMU fault identification problem by making use of the state drift calculated through the filter.

B. IMU FI Using HOSM Differentiation

So far, this Note covers the problem of maintaining performance in state estimation under input faults. This subsection explains the relationship between the drift estimator of the OTSEKF and the IMU fault identification. Recall that $\hat{\boldsymbol{f}}^i$ is the vector of IMU fault estimates, whereas $\hat{\boldsymbol{\mu}}^i$ contains estimated drift in the predicted states. Now the final part of the problem is to calculate $\hat{\boldsymbol{f}}^i$ using $\hat{\boldsymbol{\mu}}^i$, which is closely related to the flatness property of nonlinear systems.

1. *Flatness Property*

Theorem 1 ([30]): A system is considered flat if there exists an output $\boldsymbol{y}_f$ such that all states and inputs $(\boldsymbol{x}, \boldsymbol{u})$ can be expressed by the output and a finite number of its derivatives. This output is then called a flat output.

This implies that the nonlinear system defined in Eqs. (1) and (2) is only flat if the following definitions hold [10]:

$$\boldsymbol{x} = \Psi_1(\boldsymbol{y}_f, \dot{\boldsymbol{y}}_f, \ddot{\boldsymbol{y}}_f, \ldots, \boldsymbol{y}_f^{k-1}) \tag{43}$$

$$\boldsymbol{u}_m = \Psi_2(\boldsymbol{y}_f, \dot{\boldsymbol{y}}_f, \ddot{\boldsymbol{y}}_f, \ldots, \boldsymbol{y}_f^{k}) \tag{44}$$

where Ψ_1 and Ψ_2 are algebraic functions that describe smooth vector fields within the manifold, and k is the degree of differentiation. Recall the variable definitions for the nonlinear kinematic model defined in Eqs. (3–8). Based on these, it is possible to choose a candidate flat output as $\boldsymbol{y}_f = [u^b_{GS} \quad v^b_{GS} \quad w^b_{GS} \quad \phi \quad \theta \quad \psi]^T$. The advantage of this flat output choice is that the equality given in Eq. (43) is automatically satisfied as $\boldsymbol{x} = \boldsymbol{y}_f$. For the input, it is straightforward to notice that the derivatives of the flat outputs $\dot{\boldsymbol{y}}_f = [\dot{u}^b_{GS} \quad \dot{v}^b_{GS} \quad \dot{w}^b_{GS} \quad \dot{\phi} \quad \dot{\theta} \quad \dot{\psi}]^T$ are related to the measured inputs $\boldsymbol{u}_m = [A_{xm} \quad A_{ym} \quad A_{zm} \quad p_m \quad q_m \quad r_m]^T$ through algebraic relations. In essence, this means that the output is related to the states through a first-degree differentiation and algebraic relations, demonstrating that the system is flat.

Now that the system is shown to be flat, one might decompose the state and measured inputs as $\boldsymbol{x} = \boldsymbol{x}_p + \boldsymbol{\mu}^i$ and $\boldsymbol{u}_m = \boldsymbol{u} + \boldsymbol{\omega} + \boldsymbol{f}^i$, leading to the following definitions:

$$\boldsymbol{x}_p + \boldsymbol{\mu}^i = \Psi_1(\boldsymbol{y}_f, \dot{\boldsymbol{y}}_f, \ddot{\boldsymbol{y}}_f, \ldots, \boldsymbol{y}_f^{k-1}) \tag{45}$$

$$\boldsymbol{u} + \boldsymbol{\omega} + \boldsymbol{f}^i = \Psi_2(\boldsymbol{y}_f, \dot{\boldsymbol{y}}_f, \ddot{\boldsymbol{y}}_f, \ldots, \boldsymbol{y}_f^{k}) \tag{46}$$

where $\boldsymbol{\mu}^i$ represents the true drift in states caused by IMU faults. Given that $\boldsymbol{u}_m$ and $\dot{\boldsymbol{x}} = \dot{\boldsymbol{y}}_f$ have an algebraic relationship, it follows that $\dot{\boldsymbol{\mu}}^i$ and $\boldsymbol{f}^i$, which are contained within $\dot{\boldsymbol{x}}$ and $\boldsymbol{u}_m$, are similarly algebraically related.

Fundamentally, this demonstrates that it is possible to identify IMU faults simply by differentiating the drift in the state variables expressed in the body frame. However, since differentiation by nature is a noise amplifier, it is important to choose a strategy that rejects noise while maintaining accuracy.

2. *HOSM Differentiation*

According to [8], the performance of the OTSEKF degrades when the system is nonlinear and leads to significant estimation errors during the initial stage of fault identification. To overcome this, the authors proposed an iterated OTSEKF to improve the linearization of the observation model. Although this mainly resolved the deviations, close inspection reveals that even with this additional step, some spikes are observed around the initial condition. In addition, repeated linearization increases the computational load. To alleviate these problems, this study introduces a sliding-mode fault reconstruction approach. In the past, sliding mode has been applied to the inertial reference unit FDD problem [10]. However, this application only used a first-order sliding mode differentiator and did not investigate state estimation as part of the problem. In addition, the application was limited to a single fault case of a yaw-rate sensor. Hence, this section proposes higher-order sliding mode differentiation as a complementary tool to OTSEKF that allows for reconstructing IMU faults in an online setting under turbulent conditions.

Sliding mode differentiators are advantageous due to their inherent robustness to noise, high accuracy [14–16], and potentially low sensitivity to initial conditions [17]. Despite their ability to eliminate most noise, the output might exhibit low-amplitude, high-frequency oscillations. This occurs because of a phenomenon called chattering, which is the rapid discontinuous switching of the function to keep the states close to the sliding surface. A possible strategy for mitigating this is using higher-order sliding modes, where the switching action affects not only the first-order derivative but also the higher-order functions. This reduces the aggressiveness of the switching and provides a smoother derivative.

The sliding mode differentiator used in this study is given by the following set of equations in discrete and nonrecursive form:

$$\begin{aligned} z_0(t_{k+1}) = z_0(t_k) - \lambda_0 |z_0(t_k) - \hat{\mu}^i(s)|^{3/4} \mathrm{sign}(z_0(t_k) \\ - \hat{\mu}^i(s)) \Delta t + z_1(t_k) \Delta t \end{aligned} \tag{47}$$

$$\begin{aligned} z_1(t_{k+1}) = z_1(t_k) - \lambda_1 |z_0(t_k) - \hat{\mu}^i(s)|^{2/3} \mathrm{sign}(z_0(t_k) \\ - \hat{\mu}^i(s)) \Delta t + z_2(t_k) \Delta t \end{aligned} \tag{48}$$

$$\begin{aligned} z_2(t_{k+1}) = z_2(t_k) - \lambda_2 |z_0(t_k) - \hat{\mu}^i(s)|^{1/2} \mathrm{sign}(z_0(t_k) \\ - \hat{\mu}^i(s)) \Delta t + z_3(t_k) \Delta t \end{aligned} \tag{49}$$

$$z_3(t_{k+1}) = z_3(t_k) - \lambda_3 \mathrm{sign}(z_0(t_k) - \hat{\mu}^i(s)) \Delta t \tag{50}$$

where $\hat{\mu}^i(s) \in [\hat{\tilde{u}}^b_{GS} \quad \hat{\tilde{v}}^b_{GS} \quad \hat{\tilde{w}}^b_{GS} \quad \hat{\tilde{\phi}} \quad \hat{\tilde{\theta}} \quad \hat{\tilde{\psi}}]^T$ and $\lambda_{0,1,2,3}$ are chosen to achieve finite-time convergence and desirable noise rejection properties through trial and error. In this set of equations, $z_0(t_{k+1})$ gives a filtered version of $\hat{\mu}^i(s)$, which is the signal that is being differentiated; $z_1(t_{k+1})$ represents the first derivative of $z_0(t_{k+1})$ and signifies the IMU fault that is targeted for calculation. Lastly, $z_2(t_{k+1})$ and $z_3(t_{k+1})$ are the higher derivatives. Hence, the final expression for the estimated IMU faults is written as

$$z_1(t) \in \hat{\boldsymbol{f}}^i = [\hat{f}_{A_x} \quad \hat{f}_{A_y} \quad \hat{f}_{A_z} \quad \hat{f}_p \quad \hat{f}_q \quad \hat{f}_r]^T \tag{51}$$

This indicates that a fault on any of the IMU sensors is identified by differentiating the drift it causes on the corresponding state variable. The next section outlines the results of the state estimation and fault identification under turbulence.

IV. Identifying IMU Faults in Turbulent Conditions

This section presents the results of state estimation and fault identification under the effect of turbulence. It is assumed that faults in the rate gyro and linear accelerometer do not happen simultaneously. This minimizes the couplings between the faults and allows for a distinct evaluation of each fault scenario. The simulation model used in this Note belongs to the Flying-V aircraft of Delft University of Technology. The aerodynamics are represented by a 6-DOF, force-moment-based model with a linear structure given in Eq. (52).

$$C_{*} = C_{*_0} + C_{*_\alpha}(\alpha) + C_{*_\beta}(\beta) + C_{*_{p^*}}(p^*) + C_{*_{q^*}}(q^*) + C_{*_{r^*}}(r^*) + C_{*_{\delta_{CS_k}}}(\delta_{CS_k}) \tag{52}$$

where C_* stands for the force and moment coefficients C_X, C_Y, C_Z, C_L, C_M, and C_N, whereas α is the angle of attack, β is the sideslip angle, p^*, q^*, and r^* are scaled angular rates, and δ_{CS_k} denotes the control surface deflections. The aircraft has five independent control surfaces, i.e., four elevons and two coupled rudders. Further details, including the outer and inner loop characteristics, actuators, aerodynamic model, and control surface layout, can be found in [31,32]. The sensors in this model are replaced with a set of commercial off-the-shelf alternatives to achieve more realistic performance, the parameters of which are given in Table 1. Atmospheric turbulence is simulated using a Dryden turbulence model. The turbulence remains active for all the following simulations. Figure 2 gives the time histories of the turbulence components expressed in the body-fixed reference frame. For all results presented in subsequent sections, the Flying-V model is initialized from a steady-symmetric trimmed state in cruise condition.

A. Accelerometer Fault Identification

This subsection focuses on accelerometer fault identification results in turbulent flight conditions. Table 2 outlines the details of the fault scenarios. As seen in the table, there are three types of faults that act on the accelerometers for two 20 s intervals. Across all sensors, the types of faults and their magnitudes differ between intervals. The results of accelerometer fault identification are depicted in Fig. 3. For all accelerometers A_x, A_y, and A_z, the estimated faults follow the true values quite closely, indicating a successful identification. From the f_{Ax} plot, it is possible to see that even during severe oscillations in the second interval, the estimation works sufficiently fast to keep track. This indicates that the OTSEKF successfully estimates the drift in state variables and the HOSM differentiator performs a robust differentiation while retaining good exactness. Moreover, in contrast to the earlier offline application by [18], even though the filter omits the "iterated" step, the estimates remain stable and do not diverge at the beginning of the simulation. Based on these, the state estimates are expected to remain close to the true values as well because correcting the drift on the states requires accurate drift estimates. Figure 4 shows the estimated states and compares them with the measured and true states. From the figure, it is clear that all states are accurately estimated, with no noticeable drift. The measured ground speed components come from GPS measurements, which are represented in an Earth-centered, Earth-fixed frame under the assumption that Earth is flat and nonrotating. However, estimates are the ground speed components expressed in the body-fixed frame. Hence, a postestimation transformation converts them into the Earth frame to align with the sensor measurements for proper comparison.

Table 1 Sensor parameters, based on [33]

Sensor	Sampling rate, Hz	Noise standard deviation	Unit
u_{GS_m}, v_{GS_m}, w_{GS_m}	10	0.030	m/s
V_{t_m}	100	0.005	m/s
α_m, β_m	100	$2.7 \cdot 10^{-4}$	rad
ϕ_m, θ_m	100	$8.7 \cdot 10^{-5}$	rad
ψ_m	100	$1.7 \cdot 10^{-4}$	rad
A_{xm}, A_{ym}, A_{zm}	100	$6.9 \cdot 10^{-4}$	m/s^2
p_m, q_m, r_m	100	$4.1 \cdot 10^{-6}$	rad/s

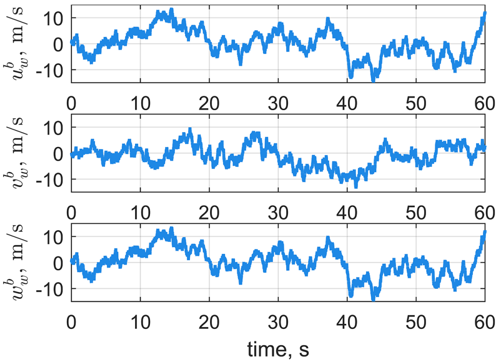

Fig. 2 Turbulent wind-speed components expressed in the body frame.

Table 2 Accelerometer fault cases

Time interval, s	Fault	Affected sensor	Magnitude	Unit
(10, 30)	Step	A_x	2	m/s^2
	Incipient	A_y	$-0.1(t-10)$	m/s^2
	Sinusoidal	A_z	$2\sin(0.5\pi t)$	m/s^2
(35, 55)	Sinusoidal	A_x	$2\sin(\pi t)$	m/s^2
	Step	A_y	1	m/s^2
	Incipient	A_z	$0.1(t-35)$	m/s^2

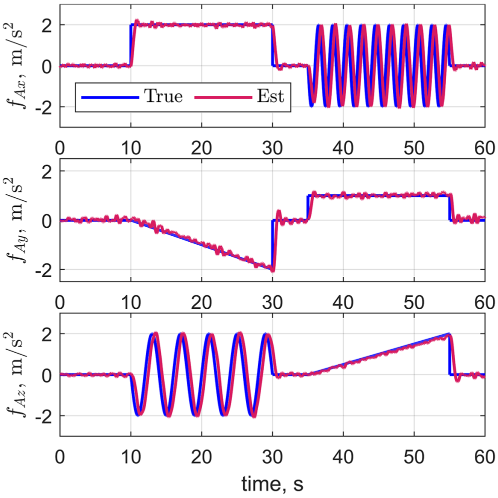

Fig. 3 True and estimated accelerometer faults.

B. Rate Gyro Fault Identification

This subsection focuses on rate gyro fault identification results in turbulent flight conditions. The fault scenarios are defined similarly to accelerometer faults and are given in Table 3. A comparison of the true and estimated gyro faults is given in Fig. 5. It is clear from the figure that the estimation of rate gyro faults is successful. One might notice that, compared to accelerometer fault estimates, gyro estimates follow the true values more closely with lower noise. This is because the attitude sensor has a significantly larger update rate than GPS and better noise characteristics. Furthermore, once again compared to the previous offline application [18], the estimates are free of divergent behavior. Figure 6 presents the estimated states and compares them with the measured and true states. Although the estimation of the attitude angles seems satisfactory, a small drift is observed in ground speed estimates. This outcome is peculiar because one might anticipate that since the gyro faults are accurately estimated, this would imply that the drift in the state variables is also estimated correctly. The explanation lies with the approximate nature of the kinematic model. From the process equations defined in Eqs. (9–14), if a fault occurs on one of the accelerometers, it does not affect the other sensors. For example, f_{Ax} only appears in $\dot{u}_{GS}^b$ as part of A_{xm} and not in any other equation. However, this is not true for gyro faults since they exhibit cross-couplings and bleed into other equations.

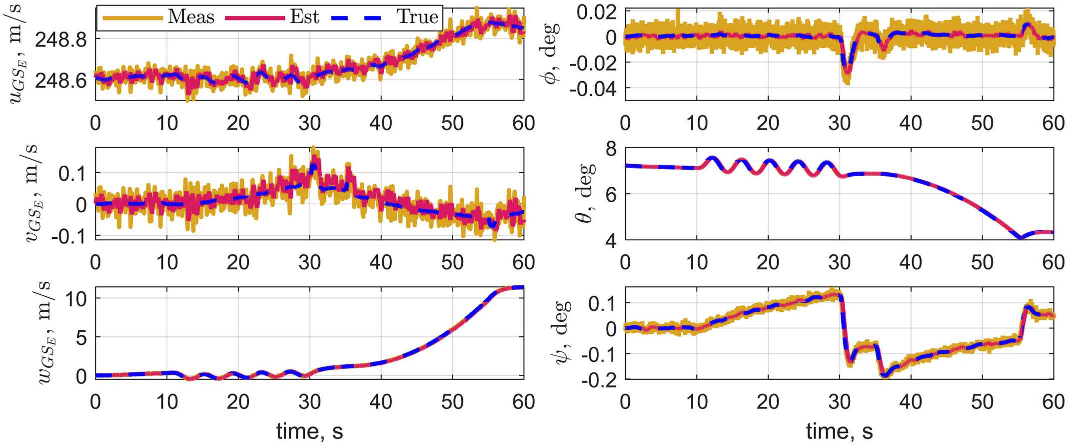

Fig. 4 Measured, estimated, and true states under accelerometer faults.

Table 3 Rate gyro fault cases

Time interval, s	Fault	Affected sensor	Magnitude	Unit
(10, 30)	Sinusoidal	p	$(\pi/180)\sin(\pi t)$	rad/s
	Incipient	q	$0.1(\pi/360)(t-10)$	rad/s
	Step	r	$-\pi/360$	rad/s
(35, 55)	Incipient	p	$-0.125(\pi/360)(t-35)$	rad/s
	Step	q	$1.5\pi/360$	rad/s
	Sinusoidal	r	$(\pi/180)\sin(0.5\pi t)$	rad/s

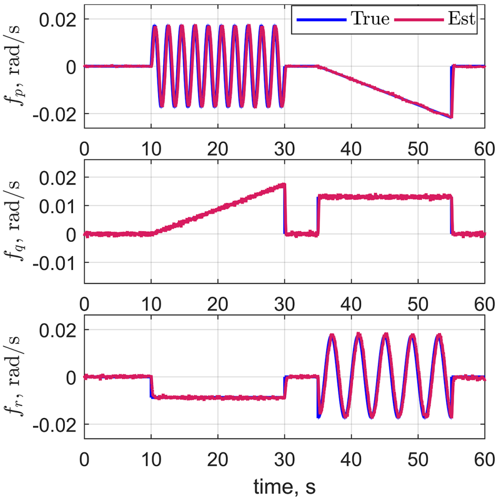

Fig. 5 True and estimated gyroscope faults.

This is due to $\hat{\boldsymbol{f}}^i$ not being exactly equal to $\boldsymbol{f}^i$, leading to some residual terms that affect the state estimation. Unlike accelerometer faults, gyro faults cause some degree of drift in all states. Cross-couplings do not cause issues in attitude angle estimation because, for a steady-symmetric flight condition in cruise, ϕ and θ are typically small; hence, the residuals diminish through trigonometric relations. Thus, the estimation remains stable, and the drift between the true and estimated states appears to be small in magnitude.

V. Active Sensor Fault-Tolerant Control System

This section combines the IMU fault identification method proposed in this Note with an INDI-based flight control system to design an active fault-tolerant flight controller for the Flying-V. The details of the Flying-V simulation model and the flight controller used in this study are available in [32,33].

INDI is a sensor-driven feedback linearization technique that uses angular acceleration feedback to derive incremental control inputs, linearizing the system. Using sensors, INDI reduces aerodynamic model dependencies and increases robustness against model mismatches. Based on [34], if the control variables are defined as angular rates $\boldsymbol{\omega} = [\,p \quad q \quad r\,]$, this leads to

$$\dot{\boldsymbol{\omega}} = \dot{\boldsymbol{\omega}}_0 + \mathbf{J}^{-1}(\mathbf{M}_\delta)\mathrm{d}\boldsymbol{\delta} \tag{53}$$

where $\mathbf{M}_\delta$ contains the moments generated by the control deflections, $\mathbf{J}$ is the moment of inertia matrix, and $\boldsymbol{\delta}$ are the control deflections. Equation (53) only holds when the time-scale separation is valid, meaning when the actuators are sufficiently fast such that the controls change much faster than the states. Defining a pseudocontrol input as $\boldsymbol{\nu} = \dot{\boldsymbol{\omega}}$ and rewriting to obtain incremental control deflections lead to the following linearizing law:

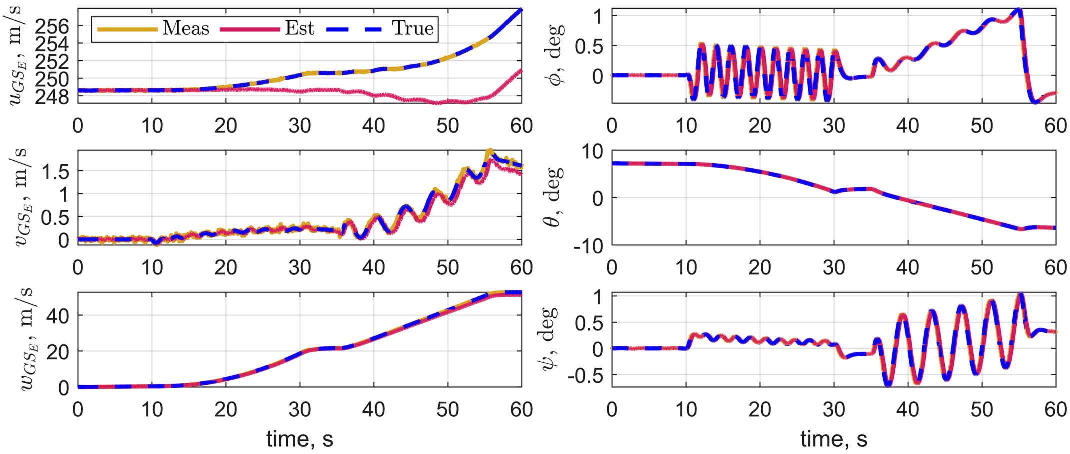

Fig. 6 Measured, estimated, and true states under gyro faults.

$$\mathrm{d}\boldsymbol{\delta} = \mathbf{M}_{\delta}^{-1}\mathbf{J}(\boldsymbol{\nu} - \dot{\boldsymbol{\omega}}_0) \tag{54}$$

This formulation assumes that $\dot{\boldsymbol{\omega}}_0$ comes either directly from the sensors or is calculated using sensory measurements. Following this, the total control deflection is computed at each step as

$$\boldsymbol{\delta}(t_{k+1}) = \boldsymbol{\delta}(t_k) + \mathrm{d}\boldsymbol{\delta} \tag{55}$$

Considering this brief INDI derivation, one may notice that, for linearization to be exact, angular acceleration measurements must be perfect, i.e., free of noise, bias, time delay, and, most importantly, faults. In addition, most aircraft, including the Flying-V model considered in this study, do not possess separate rotational accelerometers. Hence, the rotational accelerations are calculated from rate gyro measurements through differentiation. At this point, IMU fault identification and correction become highly relevant for an INDI controller because faults in rate gyros propagate into rotational accelerations through the differentiation process, causing performance degradation. To this end, this Note proposes the structure outlined in Fig. 7 to minimize the impact of IMU faults on the INDI controller.

The performance of this is assessed by comparing the response of the aircraft to the tracking commands with and without IMU fault correction. This is done separately for accelerometer and gyroscope faults using the same fault cases defined in the previous section. Based on [32], this version of the Flying-V simulation model accepts C^* for longitudinal, roll rate $\dot{\phi}$ for lateral, and sideslip β for directional commands as inputs. The C^* parameter is a combination of load factor and pitch rate, commonly defined as $C^* = n_z + (V_{CO}/g)q$. Hence, the tracking commands are chosen to be simultaneous C^* and roll rate commands to simulate a coordinated turn. Details on the nature of the tracking signals are available in [33].

A. Tracking with Accelerometer Faults

This subsection presents the results under accelerometer faults, including tracking, fault identification, and state estimation. Figure 8 shows the tracking results. From the figures, the roll rate response of the aircraft seems unaffected by the faults since both corrected and uncorrected responses are able to follow the commanded input closely. The difference is more apparent in the C^* response. The uncorrected response shows clear oscillations and drift, failing to follow the commanded input. On the other hand, although the corrected response follows the target quite nicely during the second fault interval, it also exhibits oscillations, although smaller, during the first interval. This indicates that correction of incipient and step faults is satisfactory, whereas sinusoidal faults persist even after correction.

Any fault identification approach is bound by the laws of causality, meaning that the true fault must occur first for the identification procedure to reconstruct it. For sinusoidal faults, this inevitably leads to a phase difference between the true and estimated faults. Figure 9 shows the fault identification results for the same tracking task given in Fig. 8. From the f_{Az} plot, it is seen that the estimates follow slightly behind the true values. Hence, simply removing the estimated fault from the measurement as $A_{zm} = A_z + \omega_{Az} + f_{Az} - \hat{f}_{Az}$ is not sufficient because the phase of f_{Az} is not the same as $\hat{f}_{Az}$. As a result, for sinusoidal faults, the term $f_{Az} - \hat{f}_{Az}$ leaves behind a residual signal that impacts IMU measurements. The amplitude of the residual signal is directly related to the phase shift, where smaller phase shifts lead to smaller amplitudes. Figure 10 shows the first 35 s of the f_{Az} plot and depicts the residual sinusoidal fault. As seen in the figure, even a slight phase shift is sufficient to produce a residual. Nevertheless, since the shift is not large, the residual is smaller than the true fault and leads to an

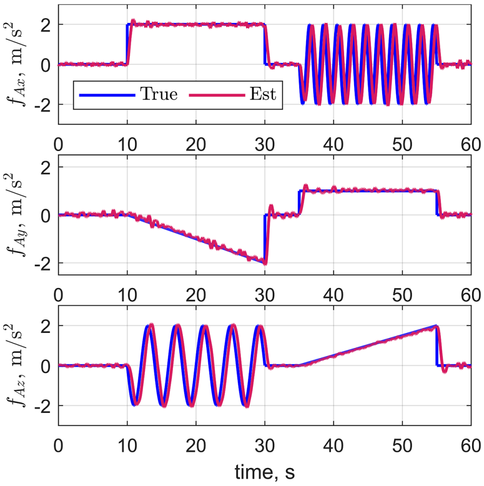

Fig. 9 Fault identification results during tracking.

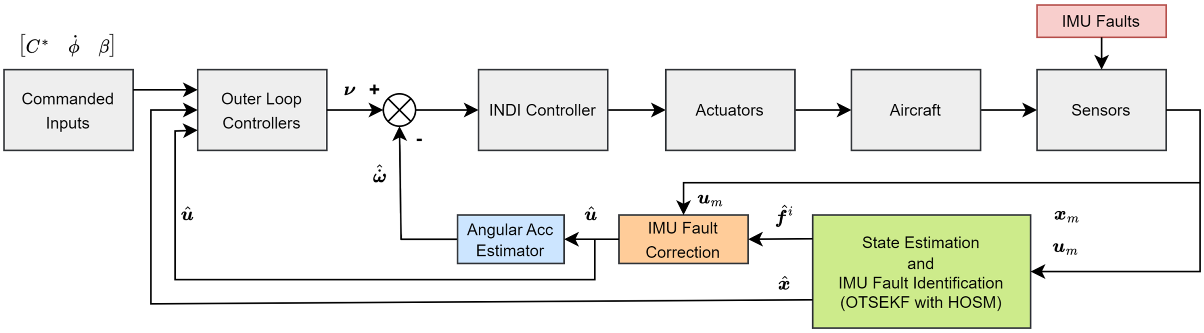

Fig. 7 Active sensor FT control structure.

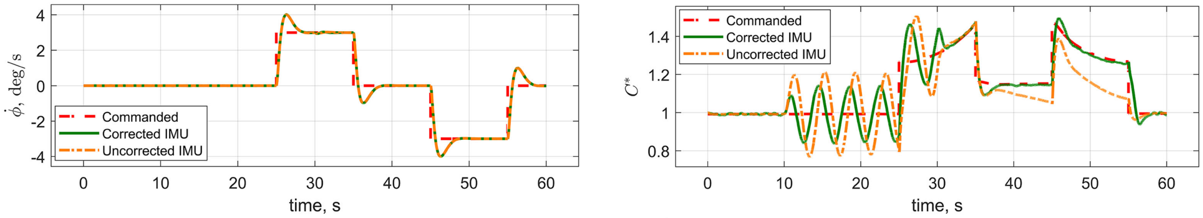

a) Roll rate responses for accelerometer faults

b) C^* responses for accelerometer faults

Fig. 8 Tracking performance under accelerometer faults.

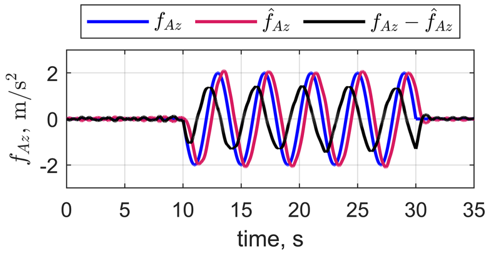

Fig. 10 True, estimated, and residual faults for sinusoidal f_{Az}.

improvement in performance, as shown in the tracking results. Since the state estimation results comparing true, measured, and estimated states are given in the previous section, they are not repeated here for conciseness.

Lastly, Fig. 11 presents the control surface deflections during tracking. None of the surfaces approach their saturation limit, which is set at ±25° for the elevons and ±30° for the rudder. However, the rudder exhibits some high-frequency, low-amplitude oscillations. This is most likely caused by the inherently approximate nature of the fault estimates and the high responsiveness of the actuator dynamics.

B. Tracking with Gyro Faults

This subsection outlines the results under rate gyro faults that include the tracking, fault identification, and state estimation. Figure 12 displays the tracking results. For rate gyro faults, the difference between the corrected and uncorrected responses becomes more apparent. Judging from the C^* response, when the faults begin acting on the rate gyros, the uncorrected response shows severe drift and offset from the commanded input. In contrast, even though it is noisier, the corrected response manages to follow the commanded signal successfully. Similarly, in roll rate tracking, the corrected response tracks the command more closely and with smaller oscillations. As explained in the previous subsection, the small oscillations remain due to residual sinusoidal faults that cannot be mitigated with IMU correction. Compared to the accelerometer fault case, the oscillations appear in the roll rate response for the gyro faults. This is due to sinusoidal faults that act on the roll rate gyroscope during the first fault interval, as shown in Fig. 13. One might notice from the fault identification results that $\hat{f}_q$ and $\hat{f}_r$ are affected by aircraft maneuvering as they show slight oscillations and underestimation. However, this effect appears to be small and does not negatively impact the results.

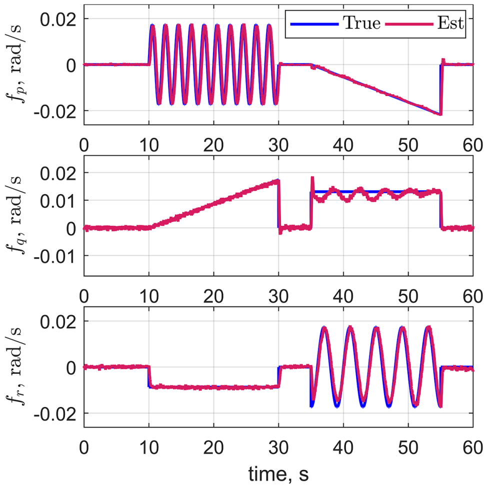

Fig. 13 Rate gyro faults during tracking.

In addition, although it is not presented here to maintain conciseness, feeding the measured states into the system instead of the estimated ones leads to a marginal decrease in the roll rate tracking performance. This occurs because the measured states come from the GPS, which operates at a lower sampling rate. Figure 6 from the previous section presents a representative comparison of the true, measured, and estimated states. The figure on control surface deflections is omitted in this section since the results appear quite similar with no saturation.

C. Comparison

This section provides a final performance comparison for tracking under accelerometer and gyroscope faults with corrected and uncorrected IMU measurements. The performance metric is chosen as the root-mean-square error between the commanded inputs and the actual response of the aircraft. The result of the comparison is given in Table 4. From this table, it is possible to notice two trends. First, for almost all tracking objectives and fault conditions, the corrected response outperforms the uncorrected, proving the effectiveness of the proposed IMU fault identification

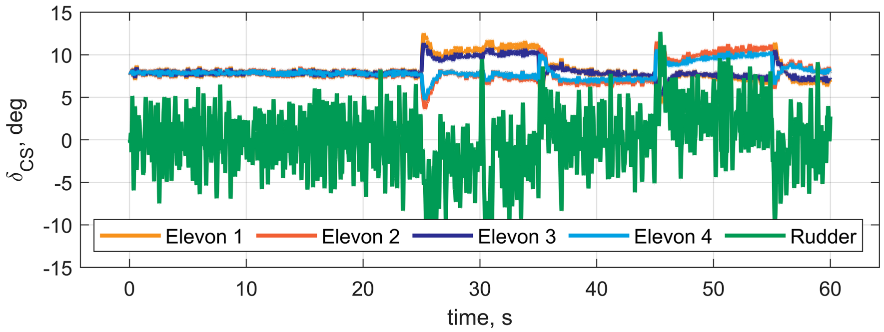

Fig. 11 Control surface deflections during tracking with accelerometer faults.

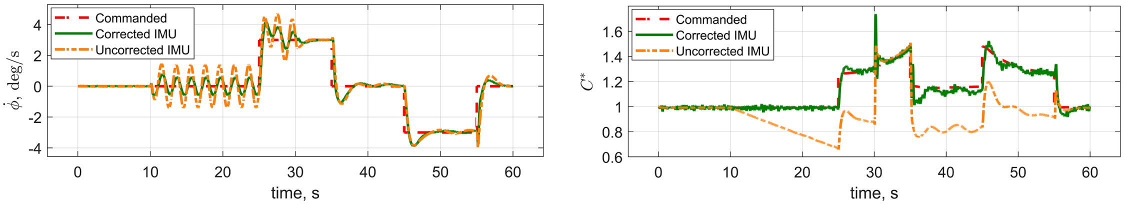

a) Roll rate responses for gyro faults **b) C^* responses for gyro faults**

Fig. 12 Tracking performance under rate gyro faults.

Table 4 Performance comparison

Affected sensors	Command	Uncorrected (RMSE)	Corrected (RMSE)
Accelerometers	$\dot{\phi}$, deg/s	0.4596	0.4596
	C^*	0.1178	0.0735
Gyroscopes	$\dot{\phi}$, deg/s	0.7526	0.5379
	C^*	0.2469	0.0487

strategy. Secondly, gyro faults appear to be more detrimental to tracking performance, since they exhibit larger RMSE values. As discussed in Sec. V, the INDI controller uses rotational accelerations to design the linearizing law. Therefore, rate gyro faults directly impact the INDI inner-loop controller.

VI. Conclusions

Online identification and mitigation of inertial measurement unit (IMU) faults is a challenging problem in flight control, especially under turbulent flight conditions without relying on hardware redundancy. The optimal two-stage extended Kalman filter (OTSEKF) with higher-order sliding mode (HOSM) differentiator effectively tackles this problem while mitigating initial condition sensitivity and noise amplification issues in IMU fault identification. The nonlinear aircraft kinematic model with nonexact process equations minimizes the cross-couplings between IMU faults and accounts for turbulence. Establishing the flatness of the kinematic model shows that IMU faults can be estimated by differentiating the drift in state variables. The results demonstrate the benefits of the suggested approach in IMU fault identification, state estimation, and aircraft response to tracking objectives. Some limitations of this strategy include sinusoidal faults leading to tracking errors due to the phase shift between the true and estimated faults and the slight deviations in state estimates caused by the approximate nature of the kinematic model.

References

[1] Zolghadri, A., "A Review of Fault Management Issues in Aircraft Systems: Current Status and Future Directions," *Progress in Aerospace Sciences*, Vol. 147, May 2024, Paper 101008.
https://doi.org/10.1016/j.paerosci.2024.101008

[2] Gao, Z., Cecati, C., and Ding, S. X., "A Survey of Fault Diagnosis and Fault-Tolerant Techniques-Part I: Fault Diagnosis with Model-Based and Signal-Based Approaches," *IEEE Transactions on Industrial Electronics*, Vol. 62, No. 6, 2015, pp. 3757–3767.
https://doi.org/10.1109/TIE.2015.2417501

[3] Accident Investigation Board, "Aircraft Accident Investigation Report, F-16CM, F-16CM, TIN 88-0479," United States Air Force, Pacific Air Forces TR, Gunsan, July 2024, https://www.afjag.af.mil/Portals/77/AIB-Reports/F-16%20_TN%2088-0479_11%20Dec%2023_AIB%20Report.pdf?ver=-V8vUaPi9gI3ClkfxDjoTw%3d%3d.

[4] "In-Flight Upset 154 km west of Learmonth, WA 7 October 2008 VH-QPA Airbus A330-303," Australian Transport Safety Bureau TR AO-2008-070, 2011, https://www.atsb.gov.au/publications/investigation_reports/2008/aair/ao-2008-070.

[5] Lombaerts, T., "Fault Tolerant Flight Control: A Physical Model Approach," Ph.D. Thesis, Delft Univ. of Technology, Delft, The Netherlands, May 2010, https://repository.tudelft.nl/islandora/object/uuid%3A538b0174-fe84-43af-954d-02f256b2ec50?collection=research.

[6] Kim, Y., Kim, I., Kim, S., and Suk, J., "Fault Diagnosis of IMU Sensor with Finite-tTime Sliding Mode Observer," *17th International Workshop on Variable Structure Systems (VSS)*, Inst. of Electrical and Electronics Engineers, New York, Oct. 2024, pp. 327–332.
https://doi.org/10.1109/VSS61690.2024.10753394

[7] He, Q., Zhang, W., Lu, P., and Liu, J., "Performance Comparison of Representative Model-Based Fault Reconstruction Algorithms for Aircraft Sensor Fault Detection and Diagnosis," *Aerospace Science and Technology*, Vol. 98, March 2020, Paper 105649.
https://doi.org/10.1016/j.ast.2019.105649

[8] Lu, P., van Eykeren, L., van Kampen, E., de Visser, C. C., and Chu, Q. P., "Aircraft Inertial Measurement Unit Fault Identification with Application to Real Flight Data," *Journal of Guidance, Control, and Dynamics*, Vol. 38, No. 12, 2015, pp. 2467–2475.
https://doi.org/10.2514/1.G001247

[9] Lu, P., van Kampen, E., de Visser, C., and Chu, Q., "Nonlinear Aircraft Sensor Fault Reconstruction in the Presence of Disturbances Validated by Real Flight Data," *Control Engineering Practice*, Vol. 49, April 2016, pp. 112–128.
https://doi.org/10.1016/j.conengprac.2016.01.012

[10] van Eykeren, L., and Chu, Q. P., "Sensor Fault Detection and Isolation for Aircraft Control Systems by Kinematic Relations," *Control Engineering Practice*, Vol. 31, Oct. 2014, pp. 200–210.
https://doi.org/10.1016/j.conengprac.2014.02.017

[11] Hajiyev, C., and Caliskan, F., *Fault Diagnosis and Reconfiguration in Flight Control Systems*, 1st ed., Vol. 2, Springer, Berlin, 2003.
https://doi.org/10.1007/978-1-4419-9166-9

[12] Ding, S. X., "Model-Based Fault Diagnosis Techniques: Design Schemes, Algorithms and Tools," *Advances in Industrial Control*, 2nd ed., Springer, London, 2013.
https://doi.org/10.1007/978-1-4471-4799-2

[13] Hsieh, C.-S., and Chen, F.-C., "Optimal Solution of the Two-Stage Kalman Estimator," *IEEE Transactions on Automatic Control*, Vol. 44, No. 1, 1999, pp. 194–199.
https://doi.org/10.1109/9.739135

[14] Levant, A., "Robust Exact Differentiation via Sliding Mode Technique," *Automatica*, Vol. 34, No. 3, 1996, pp. 379–384.
https://doi.org/10.1016/S0005-1098(97)00209-4

[15] Levant, A., Livne, M., and Yu, X., "Sliding-Mode-Based Differentiation and Its Application," *IFAC-PapersOnLine*, Vol. 50, July 2017, pp. 1699–1704.
https://doi.org/10.1016/j.ifacol.2017.08.495

[16] Levant, A., and Yu, X., "Sliding-Mode-Based Differentiation and Filtering," *IEEE Transactions on Automatic Control*, Vol. 63, No. 9, 2018, pp. 3061–3067.
https://doi.org/10.1109/TAC.2018.2797218

[17] Draženović, B., "The Invariance Conditions in Variable Structure Systems," *Automatica*, Vol. 5, No. 3, 1969, pp. 287–295.
https://doi.org/10.1016/0005-1098(69)90071-5

[18] Lu, P., and van Kampen, E., "Aircraft Inertial Measurement Unit Fault Identification with Application to Real Flight Data," *AIAA Guidance, Navigation, and Control Conference*, AIAA Paper 2015-0859, Jan. 2015.
https://doi.org/10.2514/6.2015-0859

[19] Lu, P., van Eykeren, L., van Kampen, E., de Visser, C. C., and Chu, Q. P., "Adaptive Three-Step Kalman Filter for Air Data Sensor Fault Detection and Diagnosis," *Journal of Guidance, Control, and Dynamics*, Vol. 39, No. 3, 2016, pp. 590–604.
https://doi.org/10.2514/1.G001313

[20] Friedland, B., "Treatment of Bias in Recursive Filtering," *IEEE Transactions on Automatic Control*, Vol. 14, No. 4, 1969, pp. 359–367.
https://doi.org/10.1109/TAC.1969.1099223

[21] Alouani, A., Xia, P., Rice, T. R., and Blair, W. D., "On the Optimality of Two-Stage State Estimation in the Presence of Random Bias," *IEEE Transactions on Automatic Control*, Vol. 38, No. 8, 1993, pp. 1,279–1,283.
https://doi.org/10.1109/9.233168

[22] Keller, J. Y., and Darouach, M., "Optimal Two-Stage Kalman Filter in the Presence of Random Bias," *Automatica*, Vol. 33, No. 9, 1997, pp. 1745–1748.
https://doi.org/10.1016/S0005-1098(97)00088-5

[23] Zhou, D. H., Sun, Y. X., Xi, Y. G., and Zhang, Z., "Extension of Friedland's Separate-Bias Estimation to Randomly Time-Varying Bias of Nonlinear Systems," *IEEE Transactions on Automatic Control*, Vol. 38, No. 8, 1993, pp. 1270–1273.
https://doi.org/10.1109/9.233167

[24] Mendel, J. M., "Extension of Friedland's Bias Filtering Technique to a Class of Nonlinear Systems," *IEEE Transactions on Automatic Control*, Vol. 21, No. 2, 1976, pp. 296–298.
https://doi.org/10.1109/TAC.1976.1101201

[25] Ignagni, M. B., "An Alternate Derivation and Extension of Friedland's Two-Stage Kalman Estimator," *IEEE Transactions on Automatic Control*, Vol. 26, No. 3, 1981, pp. 746–750.
https://doi.org/10.1109/TAC.1981.1102697

[26] Caglayan, A. K., and Lancraft, R. E., "A Separated Bias Identification and State Estimation Algorithm for Nonlinear Systems," *Automatica*, Vol. 19, No. 5, 1983, pp. 561–570.
https://doi.org/10.1016/0005-1098(83)90012-2

[27] Lancraft, R. E., and Caglayan, A. K., "A Fault Tolerant Approach to State Estimation and Failure Detection in Nonlinear Systems," *American Control Conference*, Inst. of Electrical and Electronics Engineers, New York, June 1982.
https://doi.org/10.23919/ACC.1982.4787964

[28] Caglayan, A. K., and Lancraft, R. E., "An Aircraft Sensor Fault Tolerant System," NASA CR 165876, April 1982, https://ntrs.nasa.gov/citations/19820017360.

[29] Alouani, A. T., Xia, P., Rice, T. R., and Blair, W. D., "Two-Stage Kalman Estimator for Tracking Maneuvering Targets," *IEEE International Conference on Systems, Man, and Cybernetics*, Inst. of Electrical and Electronics Engineers, New York, Oct. 1991. https://doi.org/10.1109/ICSMC.1991.169778

[30] Fliess, M., Levine, J., Martin, P., and Rouchon, P., "Flatness and Defect of Non-Linear Systems: Introductory Theory and Examples," *International Journal of Control*, Vol. 61, No. 6, 1995, pp. 1327–1361. https://doi.org/10.1080/00207179508921959

[31] van Overeem, S., Wang, X., and van Kampen, E., "Modelling and Handling Quality Assessment of the Flying-V Aircraft," *AIAA SciTech Forum*, AIAA Paper 2022-1429, Jan. 2022. https://doi.org/10.2514/6.2022-1429

[32] Stougie, J., Pollack, T., and van Kampen, E., "Incremental Nonlinear Dynamic Inversion Control with Flight Envelope Protection for the Flying-V," *AIAA SciTech Forum*, AIAA Paper 2024-2565, Jan. 2024. https://doi.org/10.2514/6.2024-2565

[33] Atmaca, D., and van Kampen, E., "Fault Tolerant Control for the Flying-V Using Adaptive Incremental Nonlinear Dynamic Inversion," *AIAA SciTech Forum*, AIAA Paper 2025-0081, Jan. 2025. https://doi.org/10.2514/6.2025-0081

[34] Sieberling, S., Chu, Q. P., and Mulder, J. A., "Robust Flight Control Using Incremental Nonlinear Dynamic Inversion and Angular Acceleration Prediction," *Journal of Guidance, Control, and Dynamics*, Vol. 33, No. 6, 2010, pp. 1732–1742. https://doi.org/10.2514/1.49978

M. Oppenheimer
Associate Editor